Raj Kumar[1],

Thirupathi Sirisilla[2],

M. Bharath Goud[3],

M. Harshavardhan Reddy[4],

B. Praveen[5],

M. Shiva Krishna[6]

Adaptive Hybrid Generalized Integrator based SMO For Solar PV Array Fed Encoderless PMSM Driven Water Pump

Abstract: - The increasing demand for renewable energy integration in water pumping applications has led to the development of advanced control strategies for PMSM stands for a synchronous motor powered by a permanent magnet systems. This paper presents an AHGI-based Sliding Mode Observer (SMO) for Adaptive Hybrid Generalized Integrators for sensor less control of a PMSM powered by a solar photovoltaic (PV) array. The proposed system aims to enhance efficiency, ensure robust performance under variable solar irradiance, and eliminate the need for costly position sensors. The PMSM, known for its high efficiency and reliability, requires precise rotor position and speed information for effective control. Traditional sensor-based approaches increase the overall system cost, complexity, and vulnerability to environmental factors. To address these issues, a Sliding Mode Observer (SMO) is employed for sensor less operation. However, conventional SMOs suffer from chattering and reduced accuracy under dynamic conditions. To overcome these limitations, an AHGI-based SMO is introduced, which enhances the accuracy of rotor speed and location estimate while mitigating the effects of system uncertainties and disturbances. The Generalized Adaptive Hybrid Integrator improves the low-frequency dynamic response, ensures superior noise rejection, and enables effective estimation even under varying solar irradiance and load conditions. The proposed system is powered by a solar PV array, making it highly suitable for off-grid water pumping applications. An MPPT, or maximum power point tracking algorithm optimally extracts power from the PV array, ensuring maximum utilization of available solar energy. The PMSM drive is controlled through a Field-Oriented Control (FOC) strategy, which enhances the motor's torque and speed characteristics while maintaining high efficiency. Additionally, the system employs a DC-link voltage regulator to stabilize fluctuations caused by variable solar input. A detailed comparative analysis of the proposed AHGI-SMO with conventional SMO and Extended Kalman Filter (EKF)-based estimators is executed through MATLAB/Simulink simulations and hardware implementation. The results demonstrate that the AHGI-SMO effectively reduces chattering, improves estimation accuracy, and enhances the overall dynamic response of the system. Furthermore, experimental validation confirms the robustness of the proposed method under real-world operating conditions. This research contributes to the development of cost-effective, efficient, and robust solar PV- based water pumping solutions by eliminating position sensors and improving motor control performance. The proposed AHGI-SMO framework is a promising approach for sustainable and energy-efficient agricultural and industrial water pumping applications**.**

Keywords: Encoder-less control, adaptive hybrid generalized integrator (AHGI), adaptive frequency tracker (AFT), solar water pump, and solar photovoltaic (PV) array.

1. INTRODUCTION

Significant environmental deterioration, harsh weather, and the growing depletion of crude oil supplies are some of the main issues impacting the usage of sustainable resources in power plants. Solar-powered PV systems, or photovoltaic systems, are rapidly emerging as the most competitive options due to their benefits in terms of price, effectiveness, and scalability, flexibility, and silent operation. One of the most potential uses of PV technology is water pump (WP) systems, particularly in isolated areas with limited connection to the electrical grid. WP is usually powered by an induction motor. However, because to its improved power factor, lower inertia, lower energy density, and fewer losses, PMSMs, or permanent magnet synchronous motors, are being promoted as a substitute. In order to recreate the dynamic response similar to a DC motor, a decoupled control of the torque and air-gap flux is achieved using the vector control approach, which is commonly used to regulate PMSM speed. provides a thorough examination of solutions designed specifically for salient-pole PMSM and

[1] Assistant Professor, Department of Electrical and Electronics Engineering, Marri Laxman Reddy Institute of Technology and Management, Telangana, India. Email: bommireddy210@gmail.com.

[2] Corresponding Author, Department of Electrical and Electronics Engineering, Marri Laxman Reddy Institute of Technology and Management, Telangana, India, Email: thirupathi@mlritm.ac.in.

[3] B.Tech Student, Department of Electrical and Electronics Engineering, Marri Laxman Reddy Institute of Technology and Management, Telangana, India.

[4] B.Tech Student, Department of Electrical and Electronics Engineering, Marri Laxman Reddy Institute of Technology and Management, Telangana, India.

[5] B.Tech Student, Department of Electrical and Electronics Engineering, Marri Laxman Reddy Institute of Technology and Management, Telangana, India. Email: bhanothpraveen2258@gmail.com.

[6] B.Tech Student, Department of Electrical and Electronics Engineering, Marri Laxman Reddy Institute of Technology and Management, Telangana, India.

talks about potential application areas. High power density interior PMSM (IPMSM) applications and high saturation are one possible use case for sensorless control. applications with many parameter modifications and intricate operating requirements [1].

It needs information on the position of the rotor, which is acquired via A sensor for position such as an encoder. But the encoder is susceptible to electromagnetic noise and unreliable. Additionally, it has an impact on the motor's size, weight, and cost. An ANFIS-SMO for solar PV array feeding is proposed in this article. PMSM drive without encoder for irrigation applications. This document is structured as follows [1]. Therefore, for the PMSM-driven solar WP system to be properly controlled, an encoder-less operation is required. Extended Kalman filter (EKF), sliding mode observer (SMO), disturbance observer, flux observer, and moving horizon estimation (MHE) and model reference adaptive control (MRAC) are some of the encoder-less speed controls that have been the subject of recent study. By aligning the resulting model of the system with a reference model, MRAC assesses both the rotor angle and speed. Variations in sunshine and daytime temperature, particularly in desert regions without grid access, affect the maximum PV power that may be produced. It indicates that the motor system's and the PV system's outputs must be balanced. To prevent system breakdowns brought on by abrupt reductions in irradiance, a dynamic high-speed system reaction is needed to lower the output power [2].

Parametric errors can still affect its accuracy, even if it successfully estimates the rotor's location. The underlying system states need substantial horizon evolution, notwithstanding the reliability and excellent estimation accuracy provided by MHE methods. While offering sufficient resilience, EKF necessitates high-performance CPUs and is subject to complex regulatory requirements. The flux observer and disturbance observer approaches provide inaccurate position estimations when the DC offset is applied. The coordination approach between the motor control algorithm and the ESC-based MPPT algorithm is the main emphasis of this study, which aims to keep the entire system operating. Following this format will guide the remainder of the article. A circuit that is comparable to a PV system, a negative buck converter array, and a PMSM system [2]. Furthermore, the flux observer is impacted by the motor parameter. Techniques based on SMOs are becoming more popular because to their simplicity of implementation, rapid convergence, and increased resilience.

Signum function's presence, notwithstanding its advantages, produces chattering in the SMO. Finding the necessary frequency component could be as simple as applying a filter to the input signal. It seems that a low pass filter (LPF) is the go-to choice for basic extraction. However, attenuation and phase-delay are the results. Furthermore, it causes distortion by providing a little amount of lower order harmonic (LOH) attenuation-gain. It is possible to improve system reaction time using the ESC-based MPPT method by maximizing solar panel output power minimizing output power variations under existing irradiation circumstances [2].

Adaptive notch filters are another common type of filter. Even while it greatly benefits the fundamental, it still doesn't reject LOH. There is also the adaptive-linear element (ADALINE) filter, which is rather common. It is quite effective as a filter. However, initialization, inter-harmonics, and DC offset might affect it. Although it shows great harmonic attenuation, the adaptive linear combiner is only stable at one operating frequency. The least-mean-square filter is another well-liked option. In order to manage the speed of a photovoltaic water pump (PMSM) without encoders, this study introduces an SMO based on an adaptive hybrid generalized integrator (AHGI). The solar WP system's developed AHGI structure follows a broad frequency range, eliminates dominating low-frequency components (DLOH) selectively, gives high-frequency components significant attenuation-gain, and gets rid of phase-shift and fundamental attenuation. On the other hand, it has an issue with convergence. Although it is computationally expensive, the recursive least square filter resolves this issue [3]. Harmonic mitigation has lately made use of two filters based on generalized integrators (GI): second-order GI (SOGI) and fourth-order GI (FOGI). These filters do not cause attenuation or phase delay. They are also unaffected by the DC offset. Although these harmonics reduce LOH, they are not eliminated in particular. So, when LOH are in control, they don't perform as well. To further accelerate the convergence of the inverses in the saturation sliding mode function, an exponential function reaching law is also suggested. A combined reaching law for sensor-less vector control of PMSM is then generated by merging this rule with the inverses in the saturation function [4]. Here, a hybrid generalized integrator is built with the intention of selectively removing harmonics.

Its pillars are the FOGI and the SOGI. These two filters, SOGI and FOGI, are commonly used to filter the first harmonic component of grid current. As a result, they aren't used when the frequency is highly variable. The operating frequency of a solar WP system, however, varies across a wide range due to the dynamics of solar irradiation.

In order to manage the speed of a photovoltaic water pump (PMSM) without encoders, this study introduces an SMO based on an adaptive hybrid generalized integrator (AHGI). The solar WP system's developed AHGI structure follows a broad frequency range, eliminates dominating low-frequency components (DLOH) selectively, gives high-frequency components significant attenuation-gain, and gets rid of phase-shift and fundamental attenuation. Adaptive frequency trackers (AFTs), hybrid generalized integrators (HGIs), and harmonic decoupling networks (HDNs) comprise the intended AHGI framework, which provides accurate rotor position and speed estimates. Therefore, the primary benefits of this study are: AHGI framework development. Building an AHGI-based SMO to control the speed of a solar wind turbine without using an encoder, using PMSM technology. By transforming electrical energy into mechanical energy, the PMSM turns the pump shaft to transfer water from its source to the designated location, all under the guidance of the MVC algorithm. By integrating these state-of-the-art control algorithms and simplifying system components, the proposed single-stage autonomous solar water pumping system offers several advantages over traditional water pumping systems [5]. Bode and transfer function graphs show that compared to existing methods like LPF, SOGI, and FOGI, the suggested AHGI structure is more responsive.
Using both actual and simulated back electromotive-force (EMF) helices, the benefit of AHGI over existing methods is still evident. At the same time, we have accomplished and reported the experimental performance of the AHGI-based SMO with a PMSM-driven solar WP system. Results from the tests demonstrate that the system works as expected under dynamical solar irradiation, both at startup and during steady-running, and that rotor location and speed can be precisely predicted.

1. SOLAR WP SYSTEM: COMPOSITION AND OPERATION

A PMSM-pump set, an inverter, and a PV array are designated as the main components in Fig. 1, which shows the topology at a high level. because of single-stage PV's benefits.

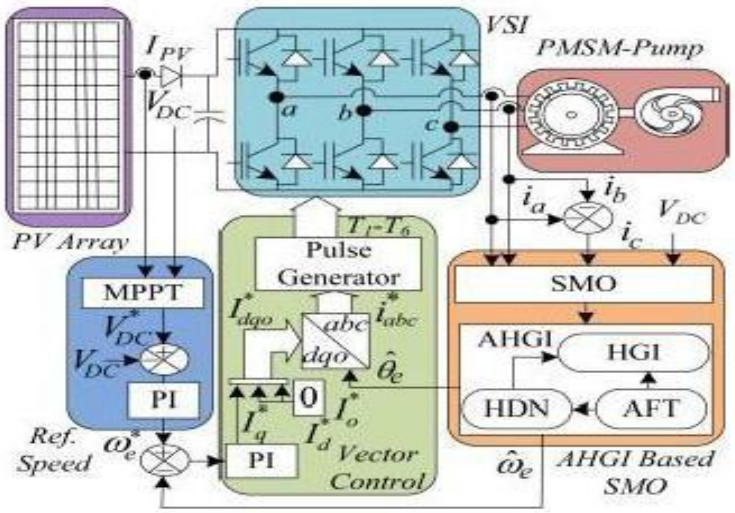

An encoder-less PMSM-powered WP solar system with an AHGI-based SMO for rotor position estimation is shown in Figure 1.

2. SMO BASED ENCODERLESS SPEED CONTROL

Here we discuss the issues with The back EMF based on SMO estimate for rotor position generation. A. Back-EMF Estimation Thinking about SMO According to the PMSM αβ-reference frame model, the β-axis is 90° electrically behind phase-a and the α-axis follows phase-a without taking into account magnetic saturation or

iron losses.

$$v_\alpha = Lpi_\alpha + Ri_\alpha + e_\alpha$$
$$v_\beta = Lpi_\beta + Ri_\beta + e_\beta$$

The sentence states that the variables p, L, vα, and eű are elements of the αβ-reference frame that voltage, current, and back-EMF, respectively, and that p is the derivative operation d/dt, resistance per phase and winding inductance, respectively. The connection between the rotor flux and αH-back EMF components is seen in Fig. 2. It follows that eα and eβ can be expressed as.

$$e_\alpha = -\lambda_{PM}\omega_e \sin\theta_e$$
$$e_\beta = \lambda_{PM}\omega_e \cos\theta_e$$

Where ωe, θe, and λPM stand for the permanent magnet's flux linkage, rotor speed, and rotor angle, in that order. As stated in (1) and (2), the SMO is made as

$$p\hat{i}_\alpha = -L^{-1}R\hat{i}_\alpha + L^{-1}\left(v_\alpha - \hat{e}_\alpha\right)$$
$$p\hat{i}_\beta = -L^{-1}R\hat{i}_\beta + L^{-1}\left(v_\beta - \hat{e}_\beta\right)$$

And

$$\hat{e}_\alpha = k.sign\left(\hat{i}_\alpha - i_\alpha\right) = k.sign\left(\Delta i_\alpha\right)$$
$$\hat{e}_\beta = k.sign\left(\hat{i}_\beta - i_\beta\right) = k.sign\left(\Delta i_\beta\right)$$

Where Given that sign is the signum function, by the following: current errors Δiα = îα - iα and Δiᵱ = îᵰ - iᵱ, gain k, and anticipated parameters "^".

$$sign\left(\Delta i_\alpha\right) = \begin{cases} +1, & \Delta i_\alpha > 0 \\ -1, & \Delta i_\alpha \le 0 \end{cases}$$

The signs (Δiα) and (Δiβ) provide the rotor angle information. As a result, the back-EMF estimate is what ultimately decides the angle of rotor. Figure 3 shows the SMO-based back-EMF estimate where the DC link voltage is denoted by VDC, the switching states of the voltage source inverter (VSI) are represented by S1–S6, and iabc = [ia ib ic] T. Where T denotes PMSM currents in phases and êαβf denotes voltages, the equation êαβ = [êαf, êβf] applies. T represents the αβ-fundamental estimated back-EMF.

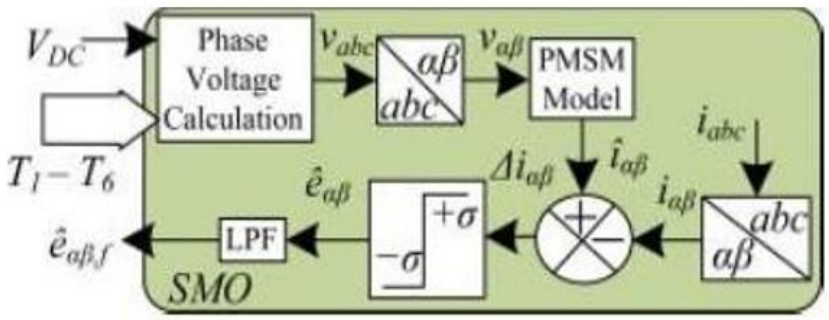

Fig. 2. SMO for back-EMF estimate with LPF.

3. POST-PROCESSING: ESTIMATED BACK-EMF BASED ROTOR POSITION GENERATION

There are discernible third-, fifth, and seventh-order harmonics in the predicted fundamental back-EMF. Here we take a look at how well FOGI, SOGI, and LPF performed for fundamental estimations in relation to Fig. 4 and its related implications. The GLPF transfer function, where the filter cut-off frequency is represented by ωc. is defined as [ωc /(jω+ωc)]. Images 4(a) and 4(d) show the block diagram and related Bode curves of LPF for ϋc = 314 rad/s, respectively. The figure shows how the LPF changes the basic back-EMF components and attenuates them. These values are -5 decibels and -45 degrees, respectively for ϋc = 314 rad/s, as shown in Figure 4(d). Consequently, the resulting rotor angle is wildly incorrect. Here is the expected location of the rotors:

$$\hat{\theta}_e = \tan^{-1}\left(\frac{\hat{e}_{\beta f}}{\hat{e}_{\alpha f}}\right)$$

We calculate the quadrature (QS) and in-phase (IS) transfer functions for the αaxis values from Fig. 4(b) of SOGI.

$$I_S = \frac{\hat{e}_{\alpha f}}{\hat{e}_{\alpha}} = \frac{jk_1\omega_c\omega}{-\omega^2 + jk_1\omega_c\omega + \omega_c^2}$$

$$Q_S = \frac{q\hat{e}_{\alpha f}}{\hat{e}_{\alpha}} = \frac{jk_1\omega_c^2}{-\omega^2 + jk_1\omega_c\omega + \omega_c^2}$$

Where The damping constant is denoted by k1. Often chosen at 0.707 taking convergence speed and stability margins into account, and The basic quadrature component of êα is qêαf. As shown in Fig. 4(e), The filtering method based on SOGI offers zero-phase shift and unity gain, improved rejection of DC offset, and superior attenuation for high frequency harmonics than LPF. However, inter-harmonics alter its reaction. The FOGI is illustrated in Fig. 4(c). Consequently, its quadrature (QF) and in-phase (IF) transfer functions are built,

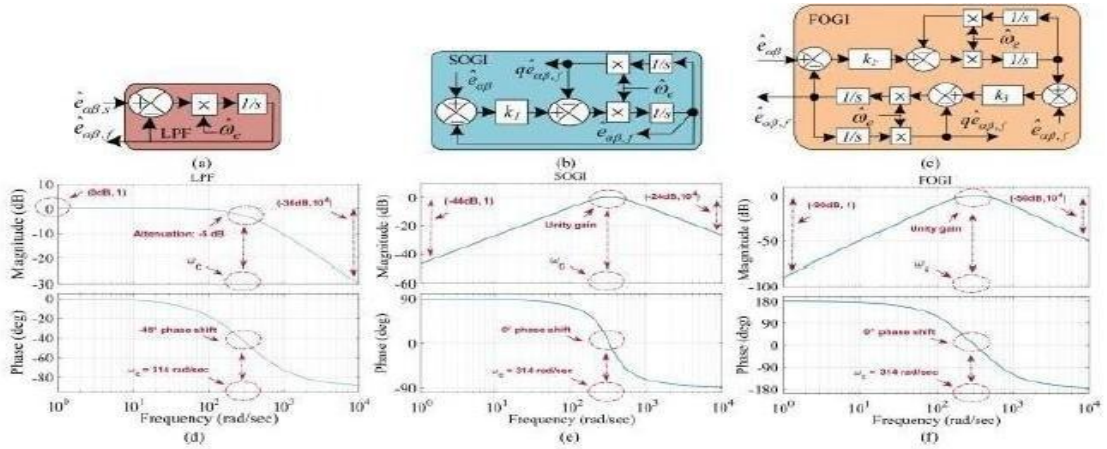

Fig 3: Back-EMF estimate using the corresponding curves of bode [(d), (e), (f)] at ωc = 314 rad/s and (a) LPF, (b) SOGI, and (c) FOGI.

$$I_F = \frac{\hat{e}_{\alpha f}}{\hat{e}_{\alpha}} = \frac{-k_2 k_3 \omega_c^2 \omega^2}{-k_2 k_3 \omega_c^2 \omega^2 + \left(-\omega^2 + jk_3 \omega_c \omega + \omega_c^2\right)\left(-\omega^2 + \omega_c^2\right)}$$

$$Q_F = \frac{q\hat{e}_{\alpha f}}{\hat{e}_{\alpha}} = \frac{jk_2 k_3 \omega_c^3 \omega}{-k_2 k_3 \omega_c^2 \omega^2 + \left(-\omega^2 + jk_3 \omega_c \omega + \omega_c^2\right)\left(-\omega^2 + \omega_c^2\right)}$$

where k2 and k3 are FOGI gains, which are determined by taking basic filtering and stability into account. Figure 4(f), which shows the Bode diagrams of FOGI, makes it clear that it performs better than SOGI in terms of high frequency attenuation characteristics and LOH rejection. Furthermore, because of its larger attenuation rate, it offers superior interharmonic weakening compared to SOGI.

Nevertheless, DLOH is not judiciously and selectively eliminated. Furthermore, changes in the cut-off frequency are not tracked by the aforementioned GIs. The purpose of the modified GIs based on phase-locked loops (PLL) is to provide them adaptability. Their application over a broad frequency range monitoring in solar WP systems is, however, restricted by the small range of their frequency tracking.

4. DEVELOPED AHGI BASED SMO FOR ENCODERLESS OPERATION OF PMSM

To overcome the drawbacks of the two GIs discussed before and make the most of their strengths, this section presents an AHGI structure that eliminates LOH and has significant high frequency attenuation.

The core elements of the proposed AHGI architecture are an adaptive frequency tracker (AFT), a hybrid decoupling network (HDN), and a hybrid generalized integrator (HGI). The HGI is the central component of the evolving AHGI structure. It consists of four stages. In the first stage, FOGI is utilized for its powerful filtering characteristics; in the subsequent three stages, SOGI is added into each one for its strong band-pass filtering feature. Stage one determines the base component of the back EMF, whereas stages two, three, and four estimate the third, fifth, and seventh harmonic signals, respectively. Subsequently, the HDN receives the fundamental and harmonic components, processes them, and outputs four distinct signals. In signals two, three, and four, the following harmonics take center stage, but in signal one, the fundamental component shines through. The four HGI stages that correspond to these signals are then communicated with. The basic component and the third, fifth, and seventh harmonics are therefore produced by the relevant steps of HGI. Also, it's worth noting that the HDN and HGI work together to remove the LOH from the input signal of the first stage FOGI. Thus, it can be concluded that HGI and HDN work together to accomplish selective harmonic elimination, as seen in Figure 5. For further information on how to choose the first stage FOGI gains, see.

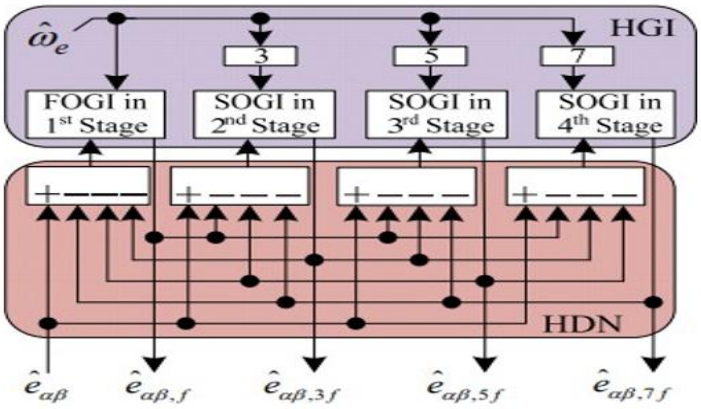

Fig. 4 Basic and DLOH estimate using HDN and HGI.

Chapter one. The gains of the second, third, and fourth stage SOGI are kept at one-third, one-fifth, and one-seventh of the first stage FOGI, respectively, in order to efficiently estimate the appropriate harmonic component.

The following is how the inphase (I) and quadrature (Q) closed loop transfer functions (TF) are derived from Fig. 5:

$$I = \frac{\hat{e}_{\alpha f}}{\hat{e}_{\alpha}} = I_F \left\{ \prod_{k=3,5,7} \frac{1 - I_{kS}}{1 - I_F I_{kS}} \right\}$$

$$Q = \frac{q\hat{e}_{\alpha f}}{\hat{e}_{\alpha}} = Q_F \left\{ \prod_{k=3,5,7} \frac{1 - Q_{kS}}{1 - Q_F Q_{kS}} \right\}$$

where, IkS and QkS for k = 3, 5, 7 are the quadrature TF and in-phase of the kth stage of SOGI. The resulting in-phase open-loop (OL) TF is as follows:

$$I_{OL} = \frac{I}{1 - I} = \frac{k_{OL} \prod_{j=1}^{12} (s + z_j)}{\prod_{i=1}^{14} (s + p_i)}$$

If kOL= k2, then pi for i = 1–14 and zj for j = 1–12 are the OL zeros and OL poles, respectively. The OL gain, denoted as For k2 = 1.5 and k3 = 3.1, k3/10 equals 0.46. Figure 6 depicts the procedure used to generate the Bode curves. At 100 rad/sec and 314 rad/sec, the phase-angle and magnitude graphs are shown in Figure 6(a) and Figure 6(b), respectively. Both the gain-margin (GM) and the phase-margin (PM) are +21 dB and +180°, respectively, at the two operating frequencies. Consequently, the AHGI possesses adequate positive stability margins and robust relative stability. The gain-crossover frequency, ϋgc, is 314 rad/s when ϋc = 314 rad/s and 100 rad/s when πc = 100 rad/s. The phase cross over frequency, ϋpc, is 890 rad/s for ϋc = 314 rad/s and 270 rad/s when ϋc = 100 rad/s. Figure 6 further indicates that the gain of the fundamental components is one, but the high frequency components decay at a rate of forty decibels per decade. The graphic clearly demonstrates the selective harmonic elimination, since it displays a considerable attenuation for the three LOHs. Additionally, the basic frequency component does not undergo any phase shift. With an attenuation of -95 dB at 1 Hz for 314 rad/sec and -83 dB at 100 rad/sec, respectively—the AHGI has strong DC offset rejection, as is seen from the

photo.

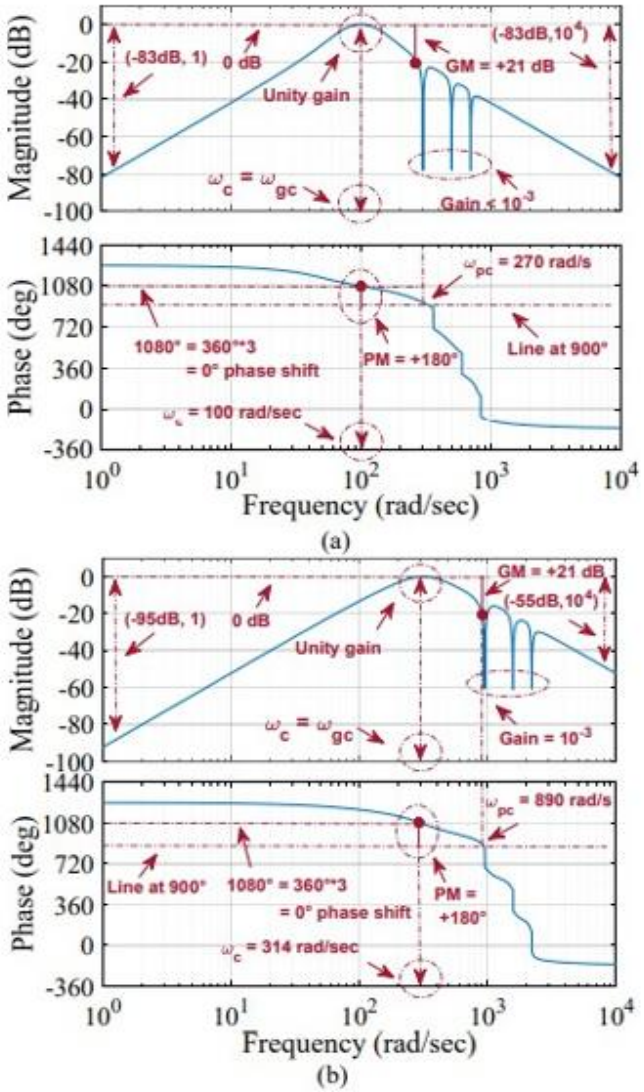

Fig. 5. HGI's bode diagram at (a) 90 rad/s and (b) 314 rad/s.

Figure 7(b) shows The block architecture of the AHGI-based SMO for rotor angle determination. The phase voltages of the PMSM, vˆabc = [vˆa vˆb vˆc] T, are calculated as [4].

$$\hat{v}_a = \{V_{DC}(2T_1 - T_3 - T_5)\}/3$$
$$\hat{v}_b = \{V_{DC}(-T_1 + 2T_3 - T_5)\}/3$$
$$\hat{v}_c = \{V_{DC}(-T_1 - T_3 + 2T_5)\}/3$$

The calculated current's αβ-components, îαβ, are found in the figure. On the basis of current error, SMO estimates the αβ-axis's back EMF. In the meantime, the AHGI reduces the basic attenuation and phase shift, adaptively traces back the EMF frequency, and successfully eliminates DLOH. Consequently, it provides a trustworthy approximation of the fundamental back-EMF elements. Consequently, a precise rotor angle is generated. Now, the back EMF estimate capacity of created AHGI, which can operate with and without harmonics, shows its superiority above FOGI, SOGI, and LPF. The comparison The outcomes of simulations are displayed in Figures 8 and 9. It should be mentioned that the The outcomes of simulations are enhances the performance of both invented and current harmonic approaches.

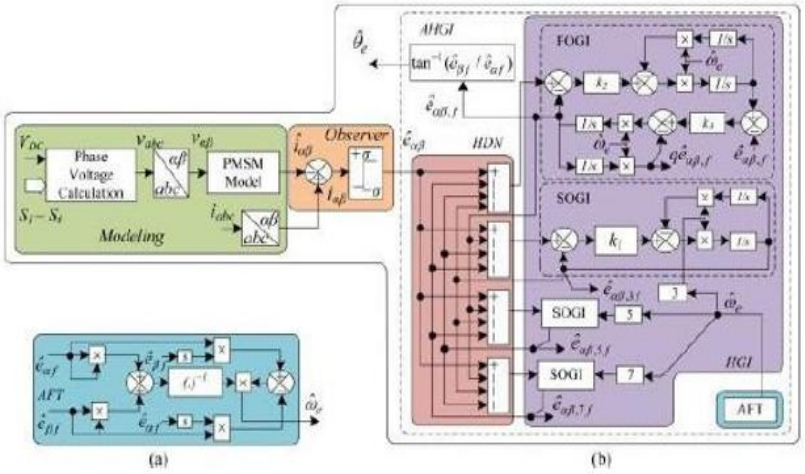

Fig. 6. Block diagram of the AHGI-based SMO that was created for the PMSM-driven solar WP system's rotor position estimate.

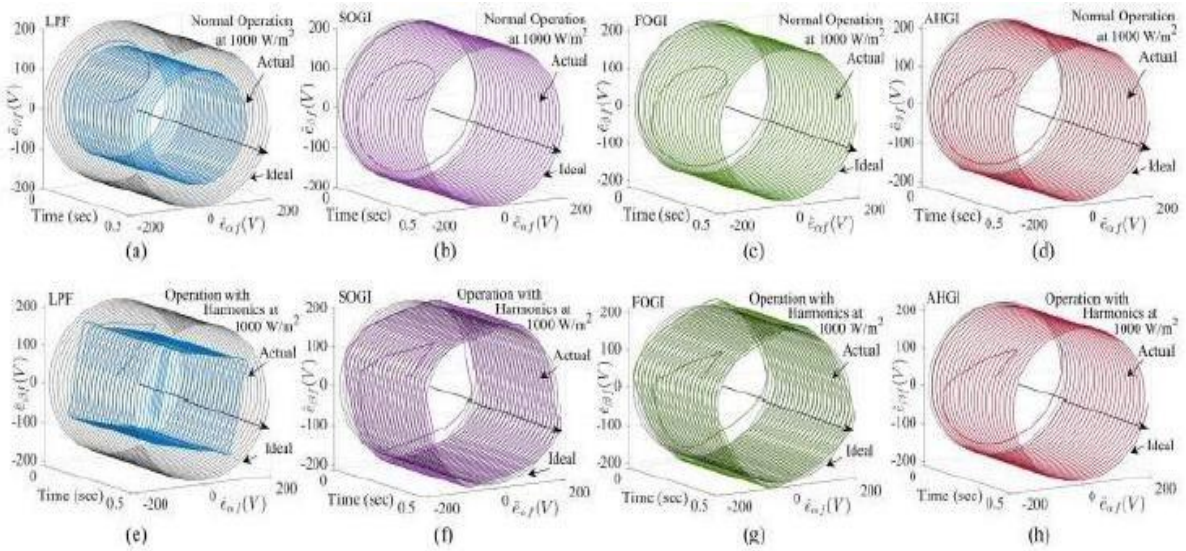

Fig. 7. Back EMF helix simulations for (a-d) regular operation and (e-h) operation with harmonics at 1 kW/m2 for (a), (e) LPF, (b), (f) SOGI, (c), (g) FOGI, and (d), (h) AHGI.

The reverse EMF helixes of four distinct techniques at 1000 W/m2 are shown in Figure 8. It appears that the back EMF produced by the LPF during normal operation has been reduced because of the decreased helix size. In this instance, the LPF helix is shown in Fig. 8(a). Nevertheless, Figs. 8(b)–(d) show that SOGI, FOGI, and AHGI generate almost optimal EMF. The LPF generated back EMF for operation with harmonics is noticeably distorted, as seen in Fig. 8(e). Its inadequate filtration is the cause of this.

Distortion arises from the real back EMF helix's departure from its pure helical structure, even if the back EMF estimate based on SOGI and FOGI is superior to LPF under harmonics. However, even under harmonics, the AHGI-based back EMF closely resembles a pure helical structure. The selective removal of harmonics is what gives AHGI its superior performance.
Even on two-dimensional back EMF trajectories, the four methods' back EMF estimating capabilities are demonstrated. During normal functioning, the back EMF circles while the harmonic EMFs do not. The decreased width of the back EMF trajectory adequately illustrates the attenuation characteristic of LPF during

both normal and harmonic operation. The generalized integrator (GI) framework is used to estimate the stationary flux components. The current literature suggests that the DC offset rejection capabilities of the standard SOGI is insufficient. Consequently, it is shown that a fourth-order GI structure may eliminate both DC offset and higher order harmonics. This study proposes an ISOGI based stator flux estimator that can reject the DC offset without reducing the predicted flux since the fourth-order structure increases processing time and computational load. Furthermore, the back EMF as determined by LPF under harmonics exhibits a discernible distortion. The proximity of the real back EMF curve to the ideal curve indicates that both the SOGI and the FOGI provide reliable back EMF estimations under normal operating conditions. However, their back EMF trajectories are severely deformed under harmonics. In contrast, AHGI uses its circular trajectory to get an accurate back EMF estimate [6].

5. EXPERIMENTAL PERFORMANCE

The suggested AHGI-based SMO for generating rotor angle and speed under the dynamics of solar irradiation is tested in a lab prototype under both starting and steady operation conditions. A comparison with existing filters, including LPF, SOGI, and FOGI, is also carried out in order to further illustrate the advantages of the developed AHGI. A PV simulator, an inverter, a DC machine, and a PMSM make up the prototype, as seen in Fig. 10. The VSI control pulses are produced by a digital signal processing unit (dS PACE). These pulses are isolated and then amplified for the gate driver of VSI switches using circuits based on bipolar junction transistors and opt couplers, respectively. Nonetheless, the Hall-effect sensors satisfy the necessary detecting requirements. A digital signal oscilloscope is used to capture pertinent signals (DSO).

In contrast, the DC power supply are utilized for the required biasing. Table I already has the specs for the main parts of the system. The experimental reactions of different system characteristics to both changing and constant sun radiation and The AHGI's rotor angle estimate and back EMF estimation performances are contrasted with those of the current techniques. The basic components of the control system hardware, which is built on fast bus technology, are an FPGA and a high-speed DSP processor (TMS320F2812). The system is capable of performing tasks including automated parameter identification, model optimization, and high-performance vector control. The next subsections provide a thorough analysis of their performances. A. Using AHGI to initiate and maintain steady-state behavior. Figure 11 shows the system's initial performance for both irradiation values using the developed AHGI-based SMO. IPV, VPV, θe, and ωe responses are shown at 1000 W/m2 and 500 W/m2, respectively [7].

Before starting, make sure the VPV is set to open circuit and the IPV is zero. Their MPP values are monitored by both of them due to the functioning of the incremental conductance method. Reduced irradiance causes a sharp drop in PV current and a small dip in PV voltage. Reason being, whereas PV voltage is logarithmic in response to irradiation, PV current is directly proportional to solar irradiation intensity.

More so, the computed speed gets closer to its steady value even when solar irradiation decreases. A good approximation of rotor angle and speed is displayed by AHGI. Also obtained are the system variables' steady-state behaviors at the two sun irradiation levels. The results of the same variables at 500 W/m2 are displayed in Figure 11(b-c). , where the back-EMF is ê = (êαf 2+êβf 2) 1/2, as well as the performance of PPV, ia, ib, ic, ϋe, êαf, êαf, and ê at 1 kW/m2. To make an adaptive fuzzy sliding mode controller, this controller combines the fuzzy control approach with the sliding mode concept. An adaptive switching gain will be generated by the adaptive fuzzy. The control law is comprised of two controls: the switching control, which stores the altered gain, and the equivalent control, which remains unchanged. At two different degrees of irradiation, the figure shows that the motor currents as well as

αβ-axes computed back EMFs are sinusoidal, indicating that the AHGI that was developed is efficient. The PMSM maintains a steady pace between the two power levels. Also, when you run AHGI continually, the system functions well. Table I [8] shows the constant values of the system parameters.

TABLE I EXPERIMENTAL VALUES OF THE VARIOUS SYSTEM PARAMETERS WITH THE DEVELOPED AHGI BASED SMO AT 1000 W/M2 AND 500 W/M2.

Parameter (Symbol)	Unit	Values	
		1000 W/m²	500 W/m²
MPP Voltage (V_{PV})	V	409	400
MPP Current (I_{PV})	A	5.7	2.9
MPP Power (P_{PV})	kW	2.33	1.16
PMSM current (i_a)	Arms	7.1	4.2
Estimated Speed (ω_e)	rad/s	157	100

Output 1:

Graph Interpretation:

1. Top Graph: DC Link Voltage (Vdc)

- The first plot remains constant at a high value (~1000V), which symbolizes the voltage of the DC connection. from the Solar PV array.
- A stable DC voltage indicates that the Maximum Power Point Tracking (MPPT) control is effectively maintaining the required power.

2. Second Graph: PMSM Stator Current (Iq or Id)

- This plot shows a decreasing pattern followed by stabilization.
- Initially, during startup, there is a higher current, which gradually decreases and stabilizes as the system reaches a steady-state condition.
- The small oscillations observed could be due to the Sliding Mode Observer (SMO) dynamics.

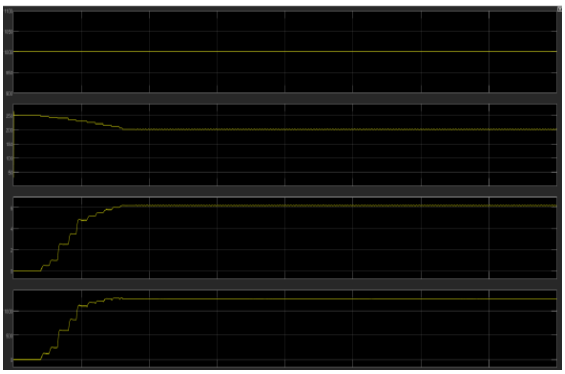

Output 2:

1. Top Graph: Stator Current (Phase Current)

- The sinusoidal waveform indicates the stator current behavior.
- Initially, the magnitude is low, and as the motor speeds up, the amplitude increases.
- The oscillations settle into a steady-state operation after a certain period.

2. Second Graph: Sliding Mode Observer (SMO) Estimated Back-EMF

- This displays the predicted signals for back-EMF from the SMO.
- The waveform has a distinct chattering effect, which is a typical characteristic of sliding mode control.
- This confirms that the SMO-based observer is working to estimate rotor position and speed.

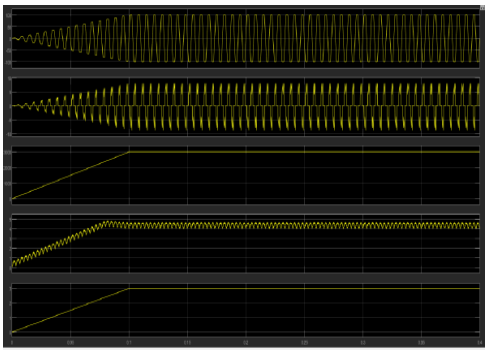

3. Third Graph: Rotor Speed (ωr)

- The velocity of the PMSM motor gradually increases from zero to its reference value.
- The smooth transition suggests a well-tuned speed controller.
- At approximately 0.12s, the speed stabilizes, indicating that the SMO-based estimation is effective.

4. Fourth Graph: Electromagnetic Torque (Te)

- The torque shows an initial increase with oscillations due to transient startup effects.
- After a short period, the torque settles to a nearly constant value, which is necessary for steady-state operation.
- The ripple in torque is due to the SMO control approach.

5. Fifth Graph: Position Estimation

- This graph represents the estimated rotor position over time.
- It shows a linear increase, confirming a continuous rotor motion.
- This validates the proper functioning of the encoder less control strategy.

The profile of several system parameters, such as VPV, IPV, ia, ib, ic, PPV, êαf, êβf, ê, etc., while the same parameters are shown with a reduction in solar irradiation. The figure shows a little decrease in VPV and a noticeable decline in IPV during irradiation fall, and vice versa. This is because of the PV array's properties. Following an irradiation modification, a seamless It is observed that all system parameters are changing to their new values. The image also shows that even during dynamics, a good approximation of the rotor location and speed is obtained. The graphic also shows a steady operation where all system parameters react appropriately, even under dynamics.

6. COMPARISON OF AHGI WITH EXISTING METHODS

The benefits of the developed AHGI over LPF, SOGI, and FOGI are demonstrated by the back EMF and rotor angle estimation performances for operation with and without harmonics. The harmonic performances are learnt when the seventh, fifth, and third harmonics are present. Back EMF curves at 1000 W/m2 were predicted by the four methods. The regular operation and harmonic operation curves, respectively. The computed back EMF by

TABLE II COMPARISON OF AHGI WITH EXISTING FILTERS

Parameter	LPF	SOGI	FOGI	AHGI
Attenuation	Yes	No	No	No
Phase-shift	Yes	No	No	No
Selective Harmonic Elimination	No	No	No	Yes
Back EMF Estimation for normal operation	Poor	Good	Good	Better
Back EMF Estimation with Harmonics	Poor	Poor	Poor	Good
Rotor Position Estimation for normal operation	Poor	Good	Good	Better
Rotor Position Estimation with Harmonics	Poor	Poor	Poor	Good

The back EMF curve's decreased width indicates that LPF attenuates for normal operation, but FOGI, AHGI, and SOGI produce accurate back EMF estimate (Figs. 13(c-d)). Additionally, as can be seen, the LPF generates a considerable distortion while operating with harmonics. Such a behavior is caused by LPF's inadequate filtering capability. However, as said, under harmonics, The FOGI and SOGI create less distortion than the LPF. Nevertheless, they also create distortion, as seen by the deviation of the optimum curve to their back EMF curves. However, as can be shown, the anticipated back EMF based on AHGI is almost perfectly round when operating with harmonics.

Therefore, even in the presence of harmonics, the AHGI generates a more accurate back EMF estimation compared to LPF, SOGI, and FOGI. The selective removal of harmonics is what gives AHGI its exceptional performance. Additionally, the AHGI's rotor angle estimate performance at 1000 W/m2 is measured and contrasted with that of the FOGI, SOGI, and LPF. The performances are shown for both regular operation and operation with harmonics. Phase-shift from the LPF results in a angle of the rotor estimate error ($e\theta$) of 0.9 rad under typical operating conditions, whereas errors from the SOGI, FOGI, and AHGI are 0.07, 0.05, and 0.03 rad, respectively respectively. This low position error is the result of AHGI's superior filtering capabilities over LPF, SOGI, and FOGI.

7. CONCLUSION

Here, we introduce SMO for encoderless PMSM based on A hybrid generalized integrator that is adaptive (AHGI) controlling a solar WP. It has been discovered that by selectively eliminating DLOH and eliminating phase-shift and fundamental attenuation, the created The AHGI structure has generated a suitable estimate of both the speed and rotor position. The frequency response and transfer function show that the AHGI structure performs better than the LPF, SOGI, and FOGI. Additionally, the predicted and experimental performances of the rotor position and back EMF have demonstrated the advantages of AHGI. It has even been possible to acquire the full experimental results of the system with the AHGI at continuous running and beginning under solar irradiation dynamics. Even under dynamics, the created AHGI structure has been demonstrated to generate a reasonable approximation of the $\alpha\beta$-components of the back-EMF. Experimental evidence has also demonstrated that the developed AHGI effectively tracks speed fluctuations. Under all operational situations, the system has demonstrated a steady and comparatively satisfactory performance. Any PMSM system may be utilized to calculate the speed and location of the rotor using the designed AHGI structure.

REFERENCES

[1] Rayapati Devi Prasad, Dr. A. Hemasekhar “Adaptive Neuro-Fuzzy Interface System-based SMO for Solar PV Array fed Encoder less PMSM Drive for Irrigation Applications” ISSN: 2395-6011 | Online ISSN: 2395-602X (www.ijsrst.com) doi:

[2] Jialiang Dai, Jungho Ahn, JuLee, HyunwooKim, SunghongWon “Acoordinated control method for static PV model fed pump motor system under rapid irradiation drop” ISSN: 17554543, DOI: 10.1049/pel2.12423

[3] M.Rezkallah , A.Chandra, M. Trembly , and H. Ibrahim, “Experimental implementation of an APC with

enhanced MPPT for standalone solar photovoltaic based water pumping station ” IEEE Trans.Subtain.Energy, vol.10,no.1,pp. 181-191, Jan.2019.

[4] Zhiqiang Liu, Wenkai Chen “Research on an Improved Sliding Mode Observer for Speed Estimation in Permanent Magnet Synchronous Motor” ISSN:10061182,

[5] Dr. Rushi Santhosh Singh Thrakur, Vusa Lakshmi Chandana, Jayampu Manasa, Manda Salmon Raju, Nallabothula Navya, Tammisetty Srikanth “Single Stage Autonomous Solar Water Pumping System using PMSM Drive” ISSN 2456 – 5083, Vol 13 Issue 04, Apr 2024

[6] Shadab Murshid, Bhim Singh “Energy-efficient single-stage solar PV powered sensorless PMSM drive for water pumping” ISSN 1752-1416,

[7] Xiong Xiao, Yongjun Zhang, Jing Wang and Haiping Du “New Adaptive Sliding-Mode Observation design for Sensorless Control of PMSM in Electric Vehicle Drive System” ISSN 1178-5608, VOL. 9, NO. 1, MARCH 2016

[8] Sabah Miqoi, Abdelghani El Ougli, Belkassem Tidhaf “Adaptive fuzzy sliding mode based MPPT controller for a photovoltaic water pumping system” ISSN: 2088-8694,